

# Euler Deconvolution applied to Potential Field Gradients

Gordon R.J. Cooper<sup>1</sup>

**Key Words:** Potential fields, semi-automatic interpretation, magnetics, gravity

## ABSTRACT

Euler deconvolution is a useful tool for providing initial estimates of the locations and depths of magnetic and gravity sources. When it has been used with aeromagnetic data, it has traditionally been applied to the total magnetic field intensity. In recent work it has been also applied to the vertical gradient of the field with much success. Its application to the horizontal gradient has been less common. This paper shows that a simultaneous deconvolution of both the horizontal and vertical gradients is robust with respect to noise. Its application to the analytic signal, a complex quantity, is also demonstrated, and shown to give superior results than those obtained from the conventional approach of the deconvolution of the amplitude of the analytic signal. Strategies for the clean computation of gradients are discussed, and a new method for rejecting invalid Euler solutions is suggested. The modified Euler deconvolution algorithm is demonstrated both on synthetic models and on aeromagnetic data from the Eastern Bushveld complex of South Africa.

## INTRODUCTION

Mineral exploration projects often require the collection of large volumes of aeromagnetic data, which then require interpretation. Various semi-automatic interpretation methods exist which are used to assist the interpreter, such as Werner deconvolution (Hartman, Teskey, and Friedberg, 1971), iSPI (Smith et al., 1998), and Euler deconvolution (Thomson, 1982; Reid et al., 1990). The methods use different physical models and produce different outputs, but in general, estimates of source depth and location will be obtained. Some methods (Mushayandebu et al., 2001) also give the dip and susceptibility of certain types of source models.

Euler deconvolution models the subsurface as a set of simple sources such as monopoles and dipoles (characterised by the structural index  $SI$ ), and it can be used to estimate the depth and location of sources of a given structural index. Example values of the structural index are 3 for a dipole and 2 for a point mass. The two-dimensional form of Euler deconvolution for a homogenous anomaly field  $f$  measured at a location  $(x, z)$  is

$$\frac{\partial f}{\partial x}(x - x_0) + \frac{\partial f}{\partial z}(z - z_0) = -SI \cdot f, \quad (1)$$

where the source location and depth are  $(x_0, z_0)$  (Thomson, 1982).

## APPLICATION OF EULER DECONVOLUTION TO POTENTIAL FIELD GRADIENTS

Applying Euler deconvolution to the vertical gradient of the magnetic or gravity field provides improved source resolution:

$$\frac{\partial}{\partial x} \left( \frac{\partial^n f}{\partial z^n} \right) (x - x_0) + \frac{\partial}{\partial z} \left( \frac{\partial^n f}{\partial z^n} \right) (z - z_0) = -(SI + n) \left( \frac{\partial^n f}{\partial z^n} \right), \quad (2)$$

where  $n$  is the order of the gradient used (which is not necessarily an integer) (Marson and Klingele, 1993; Hsu, 2002; Stavrev, 1997; Ravat et al., 2002; Cooper and Cowan, 2003). It may similarly be applied to the horizontal gradient

$$\frac{\partial}{\partial x} \left( \frac{\partial^n f}{\partial x^n} \right) (x - x_0) + \frac{\partial}{\partial z} \left( \frac{\partial^n f}{\partial x^n} \right) (z - z_0) = -(SI + n) \left( \frac{\partial^n f}{\partial x^n} \right) \quad (3)$$

(Huang et al., 1995).

Figure 1 shows a comparison of the use of Euler deconvolution using the magnetic field (Figure 1b), its 1<sup>st</sup> vertical derivative (Figure 1c), and its 1<sup>st</sup> horizontal derivative (Figure 1d). The solutions from the derivative data group much more accurately over the body corners than those from the total field. Note that the structural index used is increased by  $n$  when using a derivative of order  $n$ . This reduces the sensitivity of the solutions to the structural index used, since if the structural index is changed by an amount  $\Delta$ , the fractional change in the effective structural index is  $\Delta/SI$  if the total magnetic field is used, and  $\Delta/(SI+n)$  if the order  $n$  derivative is used. One reason why using the horizontal derivative of the field can give improved Euler solutions compared to those from the total magnetic field is that horizontal

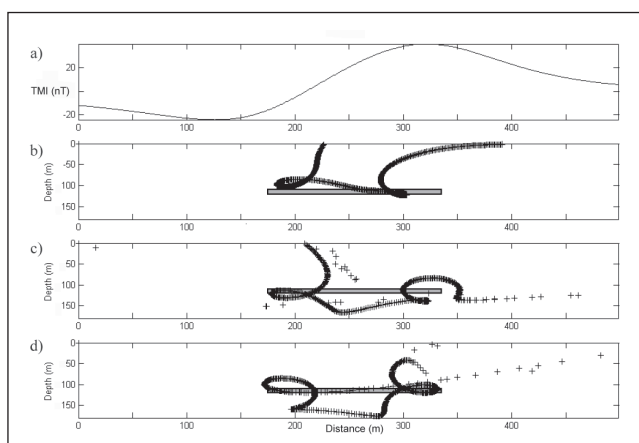


**Fig. 1.** a) Synthetic magnetic data profile generated by the body shown in Figures 1b–1d. The field inclination used was  $-60^\circ$  and the declination  $0^\circ$ . There were 500 points on the profile, spaced 1 m apart. b) Solutions from Euler deconvolution applied to the total magnetic field intensity, using a SI of 1.5 and a window size of 11 data points. All solutions are plotted. c) Solutions from Euler deconvolution applied to the first vertical derivative of the data, using a SI of 1.5 and a window size of 11 data points. All solutions are plotted. d) Solutions from Euler deconvolution applied to the first horizontal derivative of the data, using a SI of 1.5 and a window size of 11 data points. All solutions are plotted.

<sup>1</sup> School of Geosciences  
University of the Witwatersrand, Johannesburg  
South Africa 2050  
Tel: 11-7176608  
Fax: 11-7176579  
Email: cooper@geosciences.wits.ac.za, grcooper@iafrica.com

Manuscript received 21 July, 2003.

Revised manuscript received 27 July, 2004

differentiation of asymmetrical magnetic anomalies can make them more symmetrical (Cooper and Cowan, 2003). Zhang et al. (2000) applied Euler deconvolution to measured gravity tensor data and found that it improved the performance of the method: in this paper tensors are not used, and the focus is on magnetic rather than gravity data (measured gravity tensor data still being relatively scarce and expensive compared to airborne magnetic data).

The simultaneous application of Euler deconvolution to the horizontal and vertical derivatives of the field can be carried out in several different ways. Firstly, equations 2 and 3 can be solved simultaneously, i.e., equation 4 below is solved

$$\begin{bmatrix} \frac{\partial}{\partial x} \left( \frac{\partial^n f}{\partial x^n} \right) \\ \frac{\partial}{\partial z} \left( \frac{\partial^n f}{\partial z^n} \right) \end{bmatrix} (x - x_0) + \begin{bmatrix} \frac{\partial}{\partial x} \left( \frac{\partial^n f}{\partial x^n} \right) \\ \frac{\partial}{\partial z} \left( \frac{\partial^n f}{\partial z^n} \right) \end{bmatrix} (z - z_0) = -(SI + n) \begin{bmatrix} \frac{\partial^n f}{\partial x^n} \\ \frac{\partial^n f}{\partial z^n} \end{bmatrix} \quad (4)$$

Alternatively, equations 2 and 3 may be added or subtracted

$$\left( \frac{\partial^{n+1} f}{\partial x^{n+1}} \pm \frac{\partial}{\partial x} \left( \frac{\partial^n f}{\partial z^n} \right) \right) (x - x_0) + \left( \frac{\partial}{\partial z} \left( \frac{\partial^n f}{\partial x^n} \right) \pm \frac{\partial^{n+1} f}{\partial z^{n+1}} \right) (z - z_0) = -(SI + n) \left( \frac{\partial^n f}{\partial x^n} \pm \frac{\partial^n f}{\partial z^n} \right) \quad (5)$$

Since the latter form of equation 5 involves subtracting derivatives of the field, it is naturally prone to noise problems. Both equations 4 and the addition form of equation 5 were however found to be robust with respect to noise, particularly when the noise in the horizontal and vertical fields was uncorrelated. This robustness allows the use of higher order derivatives and hence produces more accurate source locations. Figures 2 and 3 compare

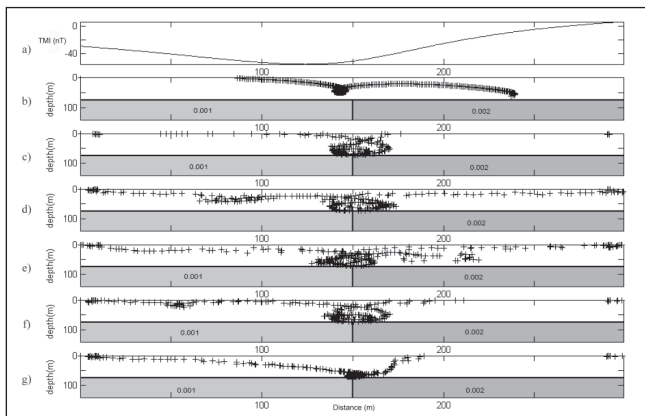


**Fig. 2.** a) Synthetic magnetic data profile generated by the model of a contact shown in Figures 2b–2g. The field inclination used was  $-60^\circ$  and the declination  $0^\circ$ . The susceptibilities used are shown on the bodies in c.g.s. units. There were 300 points on the profile, spaced 1 m apart. b) Solutions produced by the standard Euler deconvolution technique (equation 1) are shown. The SI used was 0.5 and the window size was 21 points. c) Solutions produced by the Euler deconvolution technique of the order 1.5 horizontal gradient (equation 3) are shown. The SI used was 0.5 (+2.75) and the window size was 21 points. d) Solutions produced by the Euler deconvolution technique of the order 1.5 vertical gradient (equation 2) are shown. The SI used was 0.5 (+2.75) and the window size was 21 points. e) Solutions produced by the Euler deconvolution technique applied simultaneously to the order 1.5 horizontal and vertical gradients, using the addition form of equation 5, are shown. The SI used was 0.5 (+2.75) and the window size was 21 points. f) Solutions produced by the Euler deconvolution technique applied simultaneously to the order 1.5 horizontal and vertical gradients, using the subtraction form of equation 5, are shown. The SI used was 0.5 (+2.75) and the window size was 21 points. g) Solutions produced by the Euler deconvolution technique applied simultaneously to the order 1.5 horizontal and vertical gradients, using equation 6, are shown. The SI used was 0.5 (+2.75) and the window size was 21 points.

the use of equations 1 to 5 using different source models. The order of derivative (not necessarily an integer, Cooper and Cowan, 2003) used was deliberately chosen to be sufficiently high to cause noise problems with its calculation. While higher order derivatives improve the resolution of the Euler solutions, their noise problems act in a contrary manner to degrade the resolution. Despite using order 2.75 horizontal and vertical derivatives (computed as described below), the Euler solutions from all the different approaches cluster near the contact in Figure 2, with those from equation 5 being located the most accurately. Similar results for a fault model are shown in Figure 3.

## APPLICATION OF EULER DECONVOLUTION TO THE ANALYTIC SIGNAL

An analytic signal can be formed from the gradients of the potential field, as shown in equation 6

$$A(x, z) = \frac{\partial f}{\partial x} + i \frac{\partial f}{\partial z} \quad (6)$$

(Blakely, 1995 p.352), and its amplitude is given by

$$|A(x, z)| = \sqrt{\left( \frac{\partial f}{\partial x} \right)^2 + \left( \frac{\partial f}{\partial z} \right)^2} \quad (7)$$

The application of Euler deconvolution to  $|A(x, z)|$  was suggested by Huang et al. (1995), and when this is done then the structural index must be increased by 1 compared to the value used with the total magnetic field. Salem and Ravat (2003), and Keating and Pilkington (2004) exploited the properties of the analytic signal of

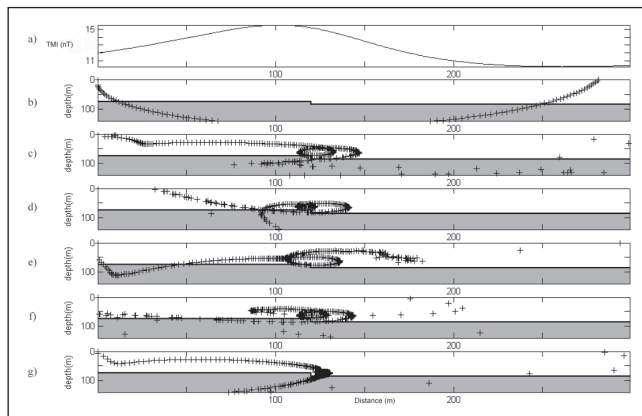


**Fig. 3.** a) Synthetic magnetic data profile generated by the model of a fault shown in Figures 3b–3g. The field inclination used was  $-60^\circ$  and the declination  $0^\circ$ . There were 300 points on the profile, spaced 1 m apart. b) Solutions produced by the standard Euler deconvolution technique (equation 1) are shown. The SI used was 0.75 and the window size was 21 points. c) Solutions produced by the Euler deconvolution technique of the order 1.5 horizontal gradient (equation 3) are shown. The SI used was 0.75 (+1.5) and the window size was 21 points. d) Solutions produced by the Euler deconvolution technique of the order 1.5 vertical gradient (equation 2) are shown. The SI used was 0.75 (+1.5) and the window size was 21 points. e) Solutions produced by the Euler deconvolution technique applied simultaneously to the order 1.5 horizontal and vertical gradients, using the addition form of equation 5, are shown. The SI used was 0.75 (+1.5) and the window size was 21 points. f) Solutions produced by the Euler deconvolution technique applied simultaneously to the order 1.5 horizontal and vertical gradients, using the subtraction form of equation 5, are shown. The SI used was 0.75 (+1.5) and the window size was 21 points. g) Solutions produced by the Euler deconvolution technique applied simultaneously to the order 1.5 horizontal and vertical gradients, using equation 6, are shown. The SI used was 0.75 (+1.5) and the window size was 21 points.

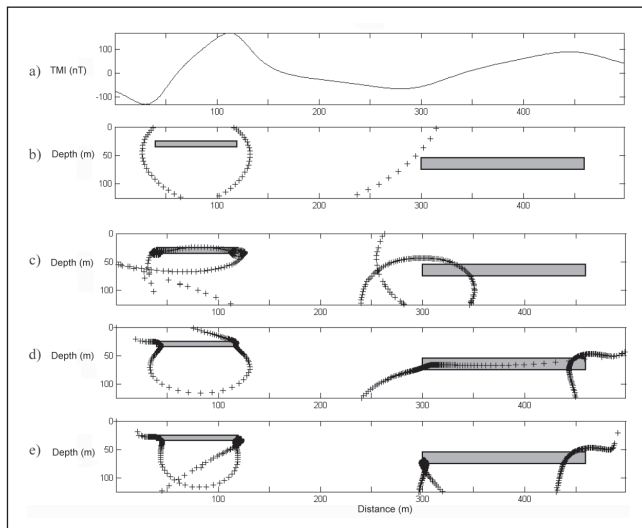


**Fig. 4.** a) Synthetic magnetic data profile generated by the bodies shown in Figures 4b–4e. The field inclination used was  $-60^\circ$  and the declination  $0^\circ$ . There were 500 points on the profile, spaced 1 m apart. b) Solutions from Euler deconvolution applied to the amplitude of the analytic signal, using a SI of 1.0 and a window size of 11 data points. All solutions are plotted. c) Solutions from Euler deconvolution applied to the 1<sup>st</sup> vertical derivative of the amplitude of the analytic signal, using a SI of 1.0 and a window size of 11 data points. All solutions are plotted. d) Solutions from Euler deconvolution applied simultaneously to the 1<sup>st</sup> horizontal gradient and the 1<sup>st</sup> vertical gradient of the data (using equation 6), with a SI of 1.0 and a window size of 11 data points. All solutions are plotted. e) Solutions from Euler deconvolution applied to the complex analytic signal, using a SI of 1.0 and a window size of 11 data points. All solutions are plotted.

simple models to obtain information on source geometry and depth, but again only the analytic signal amplitude was used. Nabighian and Hansen (2001) discuss the application of Euler deconvolution to the Hilbert transform of the magnetic field, but barely mention the analytic signal and do not discuss the simultaneous inversion of the field derivatives at all.

However, Euler deconvolution may also be applied to the complex analytic signal  $A(x, z)$  itself (when again, the structural index used must be increased by one). This is shown analytically in appendix 1 for the case of the gravity anomaly from a point source. Thurston and Smith (1998) presented an interpretation method based on wavenumbers derived from the analytic signal of the data, but their method does not involve Euler deconvolution. Figure 4 compares the application of Euler deconvolution to  $|A(x, z)|$ ,  $A(x, z)$ , and simultaneously to the 1<sup>st</sup> horizontal and vertical derivatives of the data. The solutions from the analytic signal amplitude are very diffuse compared to those from the latter methods. Applying Euler deconvolution to the 1<sup>st</sup> vertical derivative of  $|A(x, z)|$  (and using a structural index increased by 2) provided noticeably improved results compared to the application to  $|A(x, z)|$ . However, its calculation involved 3<sup>rd</sup> order derivatives and problems with noise are common when such high order derivatives are used in practice with measured field data.

The usefulness of the Euler deconvolution of the complex analytic signal is further demonstrated by its application to aeromagnetic data from the Eastern Bushveld Complex, South Africa. The profile shown in Figure 5a) comes from an aeromagnetic survey flown for the Anglo Platinum Corporation over a number of NE trending dolerite dykes which crosscut norite from the Rustenburg Layered suite. Figure 5b) shows the results of applying standard Euler deconvolution (equation 1) overlain on the modelled dyke response (Letts, pers. comm. 2003), while Figure 5c) shows the improved clustering of the Euler solutions obtained from the deconvolution of the complex analytic signal of the data.

## CLEAN COMPUTATION OF VERTICAL GRADIENTS

Equations 2 to 5 both use field gradients of order greater than one. Any noise present in the data will be amplified when its gradients are computed, because gradient filters are high pass filters. Every effort must be made to compute the gradients in as noise free a manner as possible, or the Euler deconvolution solutions will be adversely affected.

Gradients calculated in the frequency domain tend to have higher noise levels than those calculated in the space domain because of practical problems in the implementation of the Fourier transform, such as data stationarity and edge effects. The direct space domain computation of vertical gradients is impractical, but methods do exist to reduce the problem to a degree. These methods exploit the fact that horizontal derivatives are simple to calculate in the space domain, and calculate the vertical derivative from the horizontal derivatives in various ways.

The 1<sup>st</sup> horizontal derivative and the 1<sup>st</sup> vertical derivative form a Hilbert transform pair (Blakely, 1995 p.352), so the 1<sup>st</sup> vertical derivative can be calculated from the 1<sup>st</sup> horizontal derivative (calculated in the space domain) using a Hilbert transform applied in the frequency domain. This is just a rotation of the data and does not change its frequency content. The second vertical derivative can be obtained from the second horizontal derivative using Laplace's equation

$$\nabla^2 f = \frac{\partial^2 f}{\partial x^2} + \frac{\partial^2 f}{\partial y^2} + \frac{\partial^2 f}{\partial z^2} = 0 \quad (8)$$

(Blakely, 1995 p.8; Cooper, 2002).

Fedi and Florio (2001) generalised this approach to allow the stable calculation of vertical gradients of any integer order. The method has three stages. Firstly, the vertical integral of the data is calculated. Secondly, the 2<sup>nd</sup> horizontal derivatives of the vertical integral are calculated (in the space domain), and finally the required vertical derivative is obtained from Laplace's equation.

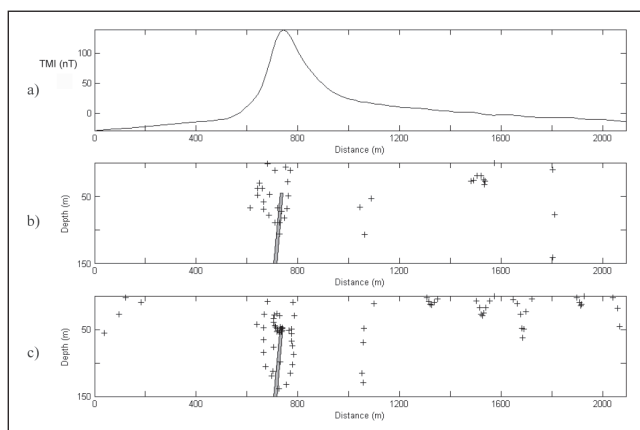


**Fig. 5.** a) Aeromagnetic data over a dyke anomaly from South Africa. There are 150 points on the profile, which is oriented  $N32^\circ W$ . The average flight height of the survey was 40m, and the flight line direction was  $359^\circ$ . The data are provided by courtesy of Mr. G. Chummet of the Anglo Platinum Corporation. b) Solutions from standard Euler deconvolution (using equation 1) are plotted over the results of modelling the aeromagnetic data. The modelling and the palaeomagnetic work performed to establish the remanent direction of the dyke magnetisation were performed by Mr. S. Letts of the School of Geosciences, University of the Witwatersrand, Johannesburg. A structural index of 1.5 was used, and all Euler solutions are plotted. c) Solutions from the Euler deconvolution of the complex analytic signal of the magnetic data shown in Figure 5a are shown. A structural index of 1.5 was used, and all Euler solutions are plotted.

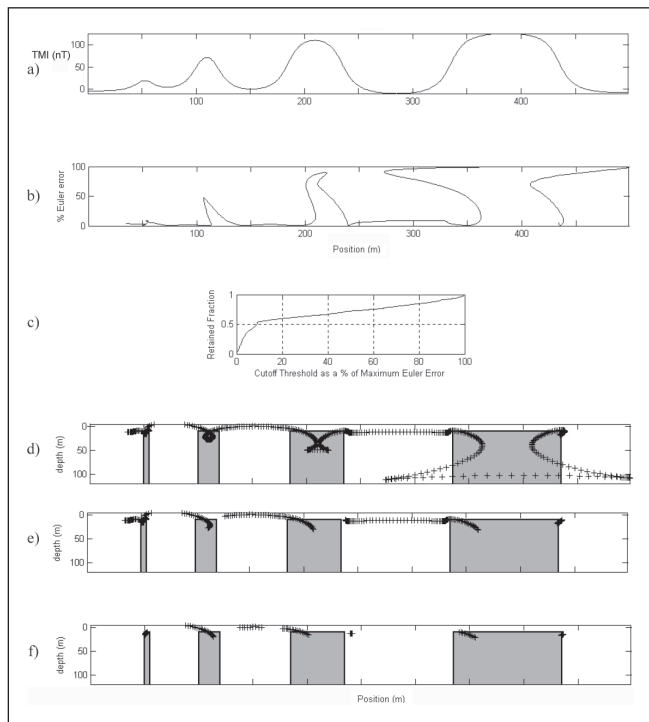


**Fig. 6.** a) Synthetic magnetic data profile generated by the 2D bodies shown in Figures 6d, 6e, and 6f. There are 500 points on the profile spaced 1 m apart, the field inclination used was  $-90^\circ$ , and the declination was  $0^\circ$ . b) Euler error (from equation 9) as a percentage of the maximum Euler error observed, as a function of distance along the profile. c) Cumulative histogram of the observed Euler error, showing the fraction of Euler solutions retained for a given cut-off threshold. d) All Euler deconvolution solutions are shown. The window size used was 31 points, and the SI was 1.5. e) Only Euler solutions corresponding to Euler errors of less than 10% of the maximum error are plotted. f) Only Euler solutions corresponding to Euler errors of less than 2% of the maximum error are plotted.

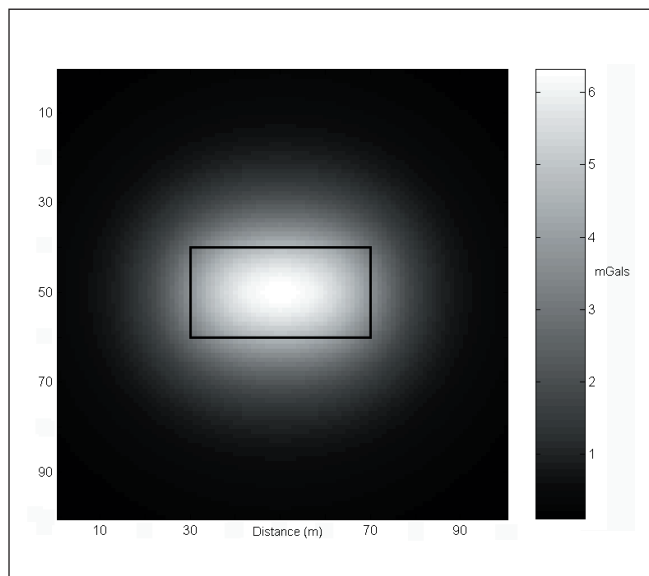


**Fig. 7a.** Gravity anomaly over a 3D rectangular body. The body location is overlain on the gravity data. Its depth extent can be seen in Figures 7b and 7c.

The procedure can be used to obtain clean vertical gradients of fractional order also. For example if the vertical derivative of order 1.75 was required, the  $2^{\text{nd}}$  horizontal derivatives of the vertical integral of order  $-0.25$  would be calculated, then these would be used to give the vertical derivative of order 1.75 (using equation 8).

### CLEAN COMPUTATION OF HORIZONTAL GRADIENTS

While integer order horizontal gradients can be easily calculated in the space domain, the calculation of clean field gradients of fractional order requires more effort. Although fractional order horizontal derivatives can be also computed in the space domain, the filters need several hundred coefficients to achieve reasonable accuracy, making them unusable in practice. However, a modification of Fedi and Florio's (2001) algorithm for the computation of integer order vertical gradients (described above) was found to be effective. To obtain a horizontal gradient of fractional order  $n$  the data was first integrated by  $m-n$ , where  $m$  is the next integer value greater than  $n$ . The  $m^{\text{th}}$  horizontal gradient of the result is then calculated in the space domain. For example, to obtain the horizontal gradient of order 0.75, the data is first integrated by order  $-0.25$  in the frequency domain, then differentiated by order 1 in the space domain. Computationally the method is not much slower than the standard frequency domain computation, because the space domain computations are rapid.

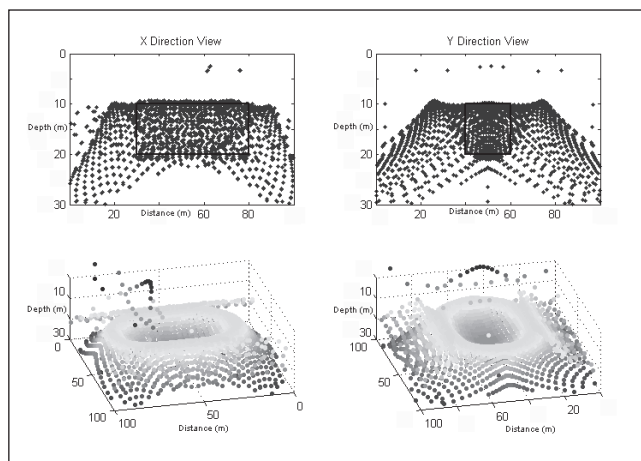


**Fig. 7b.** Euler solutions generated using a  $5 \times 5$  point window and an SI of 1. All solutions are plotted.

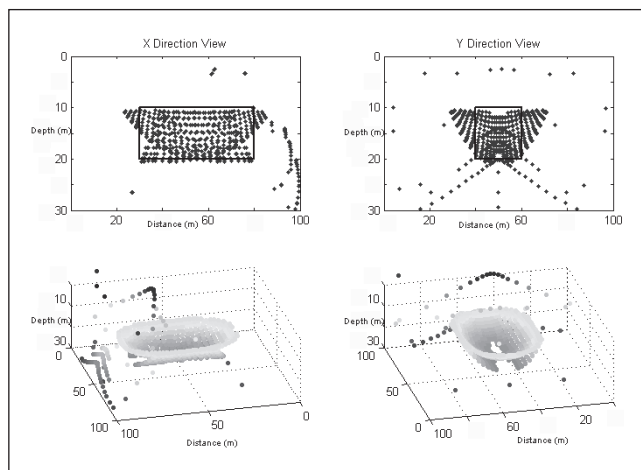


**Fig. 7c.** Only Euler solutions corresponding to Euler errors of less than 3% of the maximum error are plotted.



## REJECTION OF INVALID EULER SOLUTIONS

Euler deconvolution often generates large numbers of invalid solutions, for a variety of reasons. These include noise, interference between adjacent anomalies, and other factors such as the window size used being large enough to include data from more than one anomaly at a time. There are several strategies used to detect and remove invalid solutions. Isolated solutions (those greater than some specified distance from other solutions) may be rejected, as may solutions that lie far from the window of data points that produced them. FitzGerald et al. (2004) provide a useful summary of currently used methods.

A different approach is to examine how well Euler's equation fits the solution generated by each data point individually, i.e.,

$$Err_i = \frac{\partial f_i}{\partial x_i}(x_i - x_0) + \frac{\partial f_i}{\partial z_i}(z_i - z_0) + SI \cdot f_i \quad (9)$$

where  $(x_0, z_0)$  is the location of the Euler solution generated from a window of data points centred on  $(x_i, z_i)$ . Because a window of data points was used to generate each solution, it is not expected that the error function will be zero when calculated at a given point. However, when the error is large then problems are indicated and the solution may be rejected. The window size used should be of the order of half the anomaly size, though smaller window sizes can improve solution clustering if permitted by data noise levels. Figure 6a) shows a synthetic dataset with a small amount of added noise, and Figure 6b) shows the error function (calculated from equation 9) as a percentage of the maximum error present, at each point on the profile. Note that Figure 6b) is not a single valued function because there may be Euler solutions at several different depths for a given horizontal position (see Figures 6d), 6e), and 6f)). It can be seen that in this case the solutions with the greatest Euler error are those that lie deep beneath each body. The plot is cleaned up by rejecting solutions with an Euler error greater than a specified amount. Figure 6c) shows the cumulative histogram of the Euler deconvolution errors from the data in Figure 6a), which can be used to select the threshold value to use. For example, a cut-off value of 22% of the maximum error would remove 40% of the solutions. Figures 6d), 6e), and 6f) show the result of using different cut-off values with the dataset shown in Figure 6a). The method is not computer-intensive, the time taken being proportional to the number of solutions generated. Looking for isolated solutions by comparing the distance between each solution and all others is highly computer intensive, the time taken being proportional to the square of the number of solutions generated.

The technique was also tested on map data. Figure 7a) shows the gravity anomaly over a rectangular body, which is overlain on the anomaly. Figure 7b) shows all the Euler solutions in 2D and 3D, from different perspectives. Figure 7c) shows only the solutions with an Euler error of less than 3% of the maximum error, which account for 35.1% of the total number of solutions. A comparison of Figures 7b) and 7c) shows how the solution rejection technique has been effective in retaining those solutions which cluster near the edges of the body, and rejecting those that are located far from it, or are too deep.

## CONCLUSIONS

The application of Euler deconvolution to the gradients of potential field data, both individually and in combination, was investigated. Its application in this manner results in improved solutions compared to those from Euler deconvolution of the total field anomaly. The simultaneous Euler deconvolution of

the horizontal and vertical gradients yields improved solutions compared to either alone when noise is present in the data. The use of Euler deconvolution with the complex valued analytic signal was shown to be superior to the deconvolution of the analytic signal amplitude, and the theoretical basis for this application was proven for the case of the gravity anomaly from a point source. Clean computation of field gradients is essential for these methods to work successfully, and different strategies for achieving this were summarised and discussed. A new method for rejecting invalid solutions that improves the results and is computationally efficient was also proposed.

## ACKNOWLEDGEMENTS

Mr. S. Letts of the School of Geosciences, University of the Witwatersrand, Johannesburg, is thanked for the interpretation of the aeromagnetic data used in Figure 5, and Mr. G. Chunnet of the Anglo Platinum Corporation is thanked for his permission to use the data itself.

## APPENDIX A

Proof that Euler's Equation Holds for the Complex Valued Analytical Signal of the Gravitational Anomaly from a Point Source

The gravity anomaly of a point source is given by

$$g = \frac{GMz}{(x^2 + z^2)^{3/2}} \quad (A1)$$

(Blakely, 1995 p. 185), so

$$\begin{aligned} \frac{\partial g}{\partial x} &= -\frac{3GMzx}{(x^2 + z^2)^{5/2}} \\ \frac{\partial g}{\partial z} &= \frac{GM}{(x^2 + z^2)^{3/2}} - \frac{3GMz^2}{(x^2 + z^2)^{5/2}} \end{aligned} \quad (A2)$$

Inserting equation A2 into equation 6 in the main text gives the analytic signal response for the point source. Differentiating this with respect to both  $x$  and  $z$  and inserting into equation 1 in the main text gives

$$\begin{aligned} &GMx \left[ \frac{(12x^2z - 3z^3) + i(12xz^2 - 3x^3)}{(x^2 + z^2)^{7/2}} \right] \\ &+ GMz \left[ \frac{(-3x^3z + 12xz^3) + i(-9z^2x^2 + 6z^4)}{(x^2 + z^2)^{7/2}} \right] = \quad (A3) \\ &-(SI+1) \left[ \frac{-3GMzx}{(x^2 + z^2)^{5/2}} + i \left( \frac{GM}{(x^2 + z^2)^{3/2}} - \frac{3GMz^2}{(x^2 + z^2)^{5/2}} \right) \right] \end{aligned}$$

Collecting terms and simplifying yields

$$\begin{aligned} &\left[ \frac{(12x^3z - 3xz^3 - 3x^3z^2 + 12xz^4 + i(-3x^4 + 12x^2z^2 - 9x^2z^3 + 6z^5))}{(x^2 + z^2)^{7/2}} \right] = \quad (A4) \\ &-(SI+1) \left\{ \frac{-3zx}{(x^2 + z^2)^{5/2}} + i \left[ \frac{1}{(x^2 + z^2)^{3/2}} - \frac{3z^2}{(x^2 + z^2)^{5/2}} \right] \right\} \end{aligned}$$

so that

$$\left[ \frac{(9xz + i(-3x^2 + 6z^2))}{(x^2 + z^2)} \right] = -(SI+1) \left[ \frac{-3zx + i(x^2 - 2z^2)}{(x^2 + z^2)} \right]$$

giving  $SI = 2$ .

## REFERENCES

- Blakely, R.J., 1995, *Potential Theory in Gravity and Magnetic Applications*: Cambridge University Press.
- Cooper, G.R.J., 2002, An improved algorithm for the Euler deconvolution of potential field data: *The Leading Edge*, **21**, 1197–1198.
- Cooper, G.R.J., and Cowan, D.R., 2003, *Applications of fractional calculus to potential field data*: *Exploration Geophysics*, **34**, 51–56.
- Fedi, M., and Florio, G., 2001, Detection of potential fields source boundaries by enhanced horizontal derivative method: *Geophysical Prospecting*, **49**, 40–58.
- FitzGerald, D., Reid, A.B., and McInerney, P., 2004, New discrimination techniques for Euler deconvolution: *Computers and Geosciences*, **30**, 461–469.
- Hartman, R.R., Teskey, D.J., and Friedberg, J.L., 1971, A system for rapid digital aeromagnetic interpretation: *Geophysics*, **36**, 891–918.
- Huang, D., Gubbins, D., Clark, R.A., and Whaler, K.A., 1995, Combined study of Euler's homogeneity equation for gravity and magnetic field: *57th EAGE Conference and Technical Exhibition*, Abstracts.
- Hsu, S-K, 2002, Imaging magnetic sources using Euler's equation: *Geophysical Prospecting*, **50**, 15–25.
- Keating, P., and Pilkington, M., 2004, Euler deconvolution of the analytic signal and its application to magnetic interpretation: *Geophysical Prospecting*, **52**, 165–182.
- Marson, I., and Klingele, E.E., 1993, Advantages of using the vertical gradient of gravity for 3-D interpretation: *Geophysics*, **58**, 1588–1595.
- Mushayandebvu, M.F., van Driel, P., Reid, A.B., and Fairhead, J.D., 2001, Magnetic source parameters of two-dimensional structures using extended Euler deconvolution: *Geophysics*, **66**, 814–823.
- Nabighian, M.N., and Hansen, R.O., 2001, Unification of Euler and Werner deconvolution in three dimensions via the generalised Hilbert transform: *Geophysics*, **66**, 1805–1810.
- Ravat, D., Kirkham, K., and Hildenbrand, T.G., 2002, A source-depth separation filter: Using the Euler method on the derivatives of total intensity magnetic anomaly data: *The Leading Edge*, **21**, 360–365.
- Reid, A.B., Allsop, J.M., Granser, H., Millet, A.J., and Somerton, I.W., 1990, Magnetic interpretation in three dimensions using Euler deconvolution: *Geophysics*, **55**, 80–91.
- Salem, A., and Ravat, D., 2003, A combined analytic signal and Euler method (AN-EUL) for the automatic interpretation of magnetic data: *Geophysics*, **68**, 1952–1961.
- Smith, R.S., Thurston, J.B., Dai, T.F. and McLeod, I.N., 1998, iSPI – the improved source parameter imaging method: *Geophysical Prospecting*, **46**, 141–151.
- Stavrev, P.Y., 1997, Euler deconvolution using differential similarity transformations of gravity or magnetic anomalies: *Geophysical Prospecting*, **45**, 207–246.
- Thomson, D.T., 1982, EULDPATH: A new technique for making computer-assisted depth estimates from magnetic data: *Geophysics*, **47**, 31–37.
- Zhang, C., Mushayandebvu, M.F., van Driel, P., Reid, A.B., Fairhead, J.D., and Odegard, M.E., 2000, Euler deconvolution of gravity tensor gradient data: *Geophysics*, **65**, 512–520.